



## Quantitative imaging of solute transport in an unsaturated and undisturbed soil monolith with 3-D ERT and TDR

Johannes Koestel,<sup>1</sup> Andreas Kemna,<sup>1,2</sup> Mathieu Javaux,<sup>1,3</sup> Andrew Binley,<sup>4</sup> and Harry Vereecken<sup>1</sup>

Received 12 December 2007; revised 16 August 2008; accepted 9 September 2008; published 10 December 2008.

[1] Electrical resistivity tomography (ERT) has proved to be a valuable tool for imaging solute transport processes in the subsurface. However, a quantitative interpretation of corresponding ERT results is constrained by a number of factors. One such factor is the nonuniqueness of the ERT inverse problem if no additional constraints are imposed. In the vadose zone, further problems arise from the general ambiguity of the imaged bulk electrical conductivity in terms of water content and solute concentration. In this study we address these issues in detail for a solute tracer experiment conducted in an undisturbed unsaturated soil monolith where the tracer transport was monitored by means of 3-D smoothness-constrained ERT and time domain reflectometry (TDR) measurements. The experimental design allowed the determination of solute tracer concentrations directly from imaged bulk electrical conductivity. Independent TDR data and effluent tracer concentrations provided a “ground truth” for the ERT-derived apparent convection-dispersion equation transport parameters. The apparent transport velocity calculated from the ERT results was consistent with that based on TDR data and the sampled effluent, independent of the degree of smoothness imposed in the ERT inversion. On the other hand, the apparent dispersivity calculated from the ERT results was larger than that estimated from TDR data but smaller than that estimated from the sampled effluent, with the magnitude of deviations dependent on the degree of smoothing. Importantly, no mass balance problems were observed in the ERT results. We believe that this is largely a consequence of the uniform application of the tracer as a front and of the configuration of the electrode array with respect to the main transport direction. In conclusion, the study demonstrates that ERT can yield unprecedented quantitative information about local- and column-scale solute transport characteristics in natural soils.

**Citation:** Koestel, J., A. Kemna, M. Javaux, A. Binley, and H. Vereecken (2008), Quantitative imaging of solute transport in an unsaturated and undisturbed soil monolith with 3-D ERT and TDR, *Water Resour. Res.*, 44, W12411, doi:10.1029/2007WR006755.

### 1. Introduction

[2] The quantitative description and prediction of solute movement through the vadose zone is essential for sustainable soil and groundwater management. During the last few decades numerous studies have been carried out which contributed to this topic [Corey *et al.*, 1967; van der Pol *et al.*, 1977; De Smedt *et al.*, 1986; Vanderborght *et al.*, 2001; Javaux *et al.*, 2006] including in particular soil column experiments with well defined boundary conditions [Corey *et al.*, 1967; Mallants *et al.*, 1994; Javaux and Vanclooster, 2003]. In such studies, solute breakthrough curves (BTC) typically are measured in the column's effluent. They provide integrated and flux-averaged information on the processes governing solute transport in the

column. However, if solute displacement is sought to be understood correctly, for example, in order to make predictions, the local-scale transport properties have to be known. Here, we define the local scale as a scale smaller than the column scale for which data are available. As the local-scale transport properties cannot be measured directly in a nondestructive manner, the resident solute concentrations during inert tracer experiments can be measured instead. The local-scale apparent transport parameters can be obtained by inversely fitting analytical or numerical solutions of transport models, such as, e.g., the convection-dispersion equation (CDE), to the solute breakthrough data.

[3] Typically, two methods are used to determine resident solute concentrations in a nondestructive manner: suction cups and time domain reflectometry (TDR). Suction cups have been used for a long time in soil science to determine local-scale solute concentrations, both in the laboratory and in the field [e.g., Biggar and Nielsen, 1976; Patterson *et al.*, 2000]. However, Weihermuller *et al.* [2005] showed that suction cups modify the local matrix potential and therefore the transport paths. This method is, therefore, of limited use for a quantitative description of local solute breakthrough.

<sup>1</sup>Agrosphere ICG-4, Forschungszentrum Jülich GmbH, Jülich, Germany.

<sup>2</sup>Now at Department of Geodynamics and Geophysics, University of Bonn, Bonn, Germany.

<sup>3</sup>Department of Environmental Sciences and Land Use Planning, Université Catholique de Louvain, Louvain-la-Neuve, Belgium.

<sup>4</sup>Lancaster Environment Centre, Lancaster University, Lancaster, UK.

Although TDR was originally developed to determine soil moisture content [e.g., *Topp et al.*, 1980], the method also has been used since the 1990s to measure bulk electrical conductivity [*Heimovaara et al.*, 1995]. In this manner, breakthrough curves of resident concentrations of solutes with electrical contrast can be sampled. TDR has been shown to yield a quantitatively better insight into the heterogeneity of solute transport than suction cups [*Vanclouster et al.*, 1995; *Vanderborgh et al.*, 1997; *Javaux and Vanclouster*, 2003]. However, the method is restricted to local measurements, and the spatial resolution is therefore limited.

[4] During the 1990s, it was shown that electrical resistivity tomography (ERT) can provide a much better spatial resolution of resident solute concentrations in the course of tracer experiments than local methods such as TDR [*Binley et al.*, 1996]. A quantitative interpretation of ERT images, however, remains difficult because of several limitations related to the underlying inversion process and the diffusive nature of electrical flow [e.g., *Day-Lewis et al.*, 2005; *Kemna et al.*, 2006]. In addition, the uncertainty of inferred solute transport characteristics from ERT analysis remains ignored.

[5] An additional problem from using ERT image data arises from the fact that the bulk electrical conductivity is dependent on water content, solute concentration, and surface electrical conductivity. So, once spatially distributed bulk electrical conductivities are obtained from ERT data inversion, these conductivities have to be separated into the three contributing conductors by means of petrophysical relationships. In order to do this, information on the petrophysical model parameters and their topology is required. Such data are rarely available. Numerous studies, therefore, assume spatially constant petrophysical relationships and negligible surface conductivity [e.g., *Kemna et al.*, 2002; *French et al.*, 2002; *Winship et al.*, 2006].

[6] Several studies have been carried out using independent methods to quantitatively verify the image data obtained from ERT. Some of them investigate the ERT-derived water contents, whereas others focus on ERT-derived solute concentration. *Binley et al.* [2002] found a good quantitative agreement between cross-borehole ERT and zero-offset ground penetrating radar in terms of the velocity of the center of mass of an injected water plume. However, it was not within the scope of their study to draw conclusions about the validity of the ERT image data at the local scale. *Michot et al.* [2003], in contrast, investigated the validity of ERT image data at the local scale, although they give no statement about the validity at the bulk scale of the experiment.

[7] Among the studies which focus on solute concentration are many which confirm the qualitative agreement between results from ERT and an independent method [*Binley et al.*, 1996; *al Hagrey and Michaelson*, 1999; *Olsen et al.*, 1999; *Slater et al.*, 2000; *French et al.*, 2002]. Studies in which the validity of the ERT image data is quantitatively investigated include *Slater et al.* [2002] and *Singha and Gorelick* [2005, 2006]. *Slater et al.* [2002] compared voxel-scale ERT-derived breakthrough curves with data collected from observation wells in a solute tracer experiment under saturated conditions. They found a broad quantitative agreement in both magnitude and arrival times of the local-scale tracer pulses but dispensed with inves-

tigations at the bulk scale of the experiment. Considering the bulk scale of the experiment, *Singha and Gorelick* [2005] reported that ERT detected only 25% of the recovered mass in their field-scale tracer experiment. In a subsequent publication they investigated the corresponding local-scale ERT-derived BTCs by means of a multilevel observation well [*Singha and Gorelick*, 2006]. To our knowledge, this is the only study available in which, at the same time, both the quantitative validity of ERT images at the (voxel) local scale and at the bulk scale of the experiment have been investigated by means of an independent method.

[8] In the vadose zone, however, well-based sampling is difficult to employ. In this study we address two points which are necessary in order to investigate solute transport processes in the vadose zone quantitatively by ERT image data: (1) the bulk electrical conductivity has to be translated into solute concentration and (2) a quantitative ground truth for the ERT imaging results has to be provided at the local scale; additionally, the validity of the ERT imaging results has to be checked at the scale of the experiment if a ground truth cannot be appraised for every single voxel explicitly.

[9] Here, we present results from an experiment in which a solute tracer was applied to an undisturbed soil monolith and monitored by means of smoothness-constrained ERT and TDR as well as measurements in the effluent. The experiment was designed in a way which allowed us to relate bulk electrical conductivity to solute concentration without neglecting spatial variations in water content and mineral surface conductivity. We investigate the impact of different ERT inversion parameters on the imaging results. We contrast the (voxel-) local-scale ERT-derived bulk electrical conductivity and solute concentration with corresponding TDR data. Additionally, the shapes of the solute breakthrough curves from ERT and TDR are quantitatively compared by means of apparent transport model parameters. As a cross check of the validity of our approach at the scale of the experiment, we compare the ERT-derived apparent 1-D transport model parameters with the corresponding values determined from the effluent breakthrough data.

## 2. Experimental Setup

### 2.1. Experimental Design

[10] The experiment consists of a two step tracer test applied to a large undisturbed soil monolith under steady state unsaturated flow conditions. A constant irrigation rate of 1.5 cm/d (standard deviation 0.1 cm/d) was applied throughout the experiment. Initially, the column was irrigated with tap water and after steady state conditions had been established the tap water was replaced by a CaCl<sub>2</sub> solution (providing a positive electrical conductivity contrast) for a period of 47 days. The complete tracer breakthrough took about 30 days, although the data collection was extended to all 47 days after the tracer application (48 days in total). During the last 17 days of the experiment, chemical steady state had been established and hence the precision of the measurement devices could be checked.

[11] The temperature corrected (nLF, 25°C [see *Deutsches Institut fuer Normung*, 1993]) tap water background conductivity was adjusted to 503  $\mu\text{S}/\text{cm}$  by adding CaCl<sub>2</sub> or

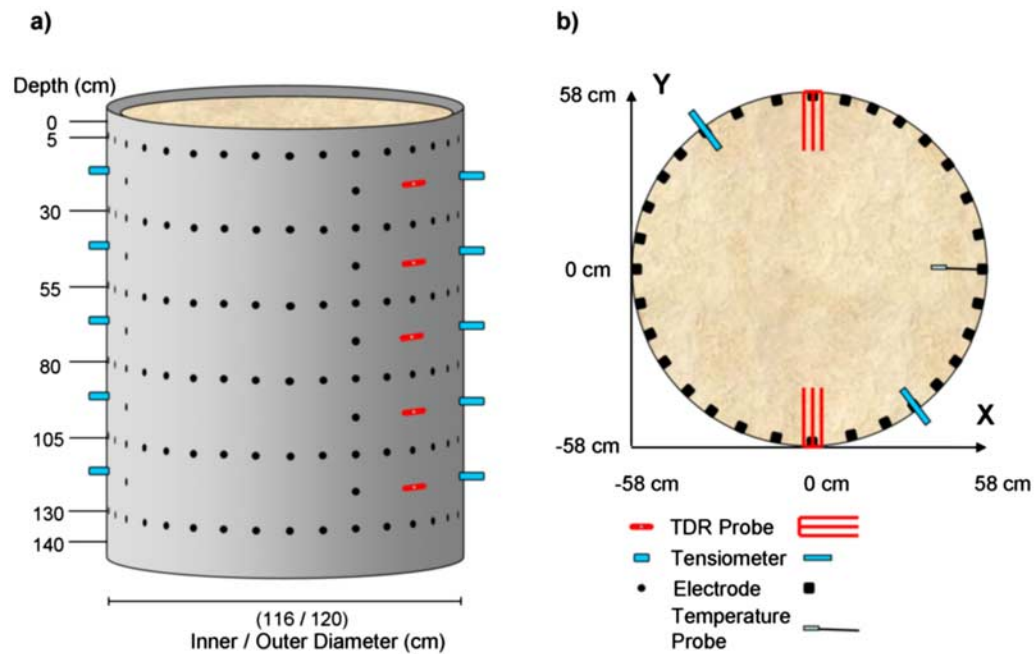


**Figure 1.** (a) Soil column and instrumentation and (b) horizontal cross section of the soil.

distilled water. This electrical conductivity was equivalent to a mean chloride concentration of 54 mg/L (standard deviation 2 mg/L). For the tracer solution, we added approximately 925 mg/L of  $\text{CaCl}_2$  adjusting the solute electrical conductivity to  $2530 \mu\text{S}/\text{cm}$ . This corresponds to a chloride concentration of 642 mg/L (standard deviation 15 mg/L). The deviations were caused by slight changes in the tap water ion composition during the experiments.

## 2.2. Soil Monolith and Soil Material

[12] We used a PVC column of 150 cm in height with an inner diameter of 116 cm and a wall thickness of 2 cm (Figure 1a) to excavate an undisturbed sandy soil monolith from an agricultural field site near Kaldenkirchen (Germany). The topmost and bottommost 5 cm of the column were not filled with the sample: at the bottom, the corresponding gap was backfilled with sand; at the top, the soil surface was covered with a thin layer of fine gravel in order to prevent erosion caused by irrigation.

[13] In total, 212 stainless steel electrodes (1.2 cm in diameter) were installed extending 3 cm into the soil, respectively. The majority of the electrodes (192) were arranged equidistantly along the circumference of the soil column with a horizontal spacing of 11.8 cm in six different depths (Figure 1a). Additionally, five electrodes were placed vertically in between each of the six electrode rings along four vertical transects. We used a six-channel GeoServe RESECS with corresponding relay boxes to carry out the ERT measurements.

[14] In addition to the ERT electrodes, ten TDR probes were inserted into the column. The TDR probes were positioned diametrically opposed to each other at five different depths (Figures 1a and 1b). We used a three-rod design similar to the one employed by *Heimovaara* [1993]. We chose a rod length of 18.8 cm and a rod spacing of 2.5 cm. The rod spacing to diameter ratio was 10:1. The TDR signals were generated and recorded by

means of a Campbell Scientific TDR100 system. The dielectric constant as well as the signal attenuation was logged at 1 h intervals using Campbell Scientific SDMX50 multiplexers and a Campbell Scientific CR10X data logger. In order to avoid electricity short cuts through the TDR cables (and therefore artifacts in the ERT images), switches were built in between TDR probes and multiplexers. In this way, we were able to electrically isolate the TDR probes from each other whenever ERT measurements were performed. Thus, we could apply both methods, ERT and TDR, simultaneously although they had to be alternately switched on and off.

[15] Next to each TDR probe a tensiometer (UMS T4) was installed (see Figure 1b). The tensiometer data were logged every ten minutes with aid of a MAC19 data logger. In addition, a resistance temperature detector (PT100) was installed in each TDR/tensiometer plane.

[16] In order to discriminate between the two vertical TDR and tensiometer transects, they are, in the following, referred to by their XY coordinates (0|58) and (0|-58) in centimeter.

## 2.3. Boundary Conditions

[17] The experiment was performed in a basement of the lysimeter facility of the Forschungszentrum Jülich. The ambient temperature was kept around  $10^\circ\text{C}$  ( $\pm 2^\circ\text{C}$ ) to minimize temperature effects on the electrical conductivity. An irrigation device, consisting of a reservoir with 484 needles, was placed on top of the soil column, allowing spatial uniformity of the irrigation. The soil column was mounted on a balance in order to verify steady state conditions. The lower section of the soil column was water saturated during the experiments.

[18] Twelve openings in the bottom section of the column allowed discharge to a 100 mL tipping bucket (UGT Müncheberg). The flow rate was measured and logged on the MAC19 data logger. The effluent was conducted

**Table 1.** Dielectric Numbers  $\xi$  Which We Used to Calculate the Water Content at the TDR Positions<sup>a</sup>

$\xi_{s,topsoil}$	$\xi_{s,subsoil}$	$\xi_a$	$\xi_w$
5	3.9	1	84.3

<sup>a</sup>The indices  $s$ ,  $a$ , and  $w$  stand for solid phase, air, and water, respectively;  $\xi_w$  is for 9.5°C.

through a vessel where the electrical conductivity and the water temperature were measured at 10 min intervals by a WTW Condi325 conductivity meter.

### 3. Methods

#### 3.1. TDR Measurements

[19] The TDR data were used to measure the water content,  $\theta$  ( $\text{cm}^3/\text{cm}^3$ ), as well as the bulk electrical conductivity. For the water content measurement, the bulk dielectric constant  $\xi_b$  (-) was used to infer water content using the composite dielectric approach [Roth *et al.*, 1990]:

$$\theta = \frac{\xi_b^\alpha - (1 - \Phi)\xi_s^\alpha - \Phi\xi_a^\alpha}{\xi_w^\alpha - \xi_a^\alpha}. \quad (1)$$

Here,  $\xi_s$ ,  $\xi_a$ , and  $\xi_w$  refer to the temperature corrected dielectric constant of soil solid, air, and water phase, respectively, and  $\Phi$  is the porosity. The corresponding values were taken from Roth *et al.* [1990]. They are listed in Table 1. The geometry factor  $\alpha$  was set to 0.5, which corresponds to the Complex Refractive Index Model (CRIM) [e.g., West *et al.*, 2003].

[20] The bulk electrical conductivity  $\sigma_b$  ( $\mu\text{S}/\text{cm}$ ) was obtained from the TDR signal attenuation for measurement times much greater than the main detection of the reflected signal. We related the signal attenuation to the bulk electrical conductivity of the soil in the vicinity of the TDR rods using the relationship

$$R_{TDR} = Z_C \frac{(1 + \rho_\infty)}{(1 - \rho_\infty)}. \quad (2)$$

Here,  $\rho_\infty$  is the reflection coefficient at very long times, and  $Z_C$  is the impedance of the TDR device, multiplexer, and cable.  $R_{TDR}$  is the ensemble resistance of  $Z_C$  and the resistance of the bulk soil [Heimovaara *et al.*, 1995; Mallants *et al.*, 1996]. This then permits estimation of the bulk electrical conductivity according to

$$\sigma_b = \frac{K_p}{R_{TDR} - R_{Cable}}. \quad (3)$$

Here,  $K_p$  is the cell constant of the TDR probe, and  $R_{Cable}$  is the resistance associated with cable tester, multiplexers, and connectors.

[21] Both  $K_p$  and  $R_{Cable}$  were determined for each probe individually using calibration measurements. Therefore, the signal attenuation was measured for TDR probes immersed in water with a known electrical conductivity. The measurements were carried out for eight different electrical conductivities ranging from 11.6  $\mu\text{S}/\text{cm}$  to 618  $\mu\text{S}/\text{cm}$ . For the calibration process, the mean absolute residuals  $\langle R \rangle$

were below 1  $\mu\text{S}/\text{cm}$ . Given the bulk electrical conductivities which we measured during the experiment (25–300  $\mu\text{S}/\text{cm}$ ), we can infer a TDR accuracy of 0.3 to 4%. This is in the range of the accuracy of TDR electrical conductivity measurements published by Huisman *et al.* [2008].

[22] After the TDR probes were installed, the precision of the TDR electrical conductivity measurements was investigated under hydraulic and chemical steady state conditions. We found the coefficient of variation for the electrical conductivity measurements collected during 10 consecutive days to be below 2% for all TDR probes, with a mean coefficient of variation of approximately 1%. The precision of the TDR system is hence rated as high.

#### 3.2. ERT Imaging

##### 3.2.1. Inversion Algorithm

[23] We carried out 3-D ERT inversions to map changes in the spatial distribution of bulk electrical conductivity  $\sigma_b$  ( $\mu\text{S}/\text{cm}$ ) inside the soil monolith. We performed 46,260 “skip one” dipole-dipole measurements (see Slater *et al.* [2000] for more details on this configuration) for each measurement frame (50% of which were reciprocal measurements, where current and potential dipoles are switched, in order to assess data quality). We used dipole-dipole configurations with both horizontal and vertical dipoles. The dipole length was 22.8 cm for the horizontal scheme and 25 cm for the vertical schemes. The measurement time for one complete measurement frame was 8 h and 23 min. One frame per day was recorded. We inverted the ERT data for each frame individually by means of the error-weighted, smoothness-constrained “Occam’s type” inversion code R3t. No time-lapse regularization was applied. The code utilizes a triangular prism-based finite element solution of the forward problem [Binley *et al.*, 1996] and has been previously demonstrated for soil core experiments by Olsen *et al.* [1999]. The algorithm finds the smoothest distribution of electrical conductivity which fits the measured data to a specified error level  $\varepsilon_{app}$  using the approach described by Binley and Kemna [2005].

[24] The ERT inversion produces an image of  $M$  voxel electrical conductivities ( $\sigma_j, j = 1, 2, \dots, M$ ) given a set of  $N$  measurements of four-electrode resistance ( $R_i, i = 1, 2, \dots, N$ ) by minimizing the objective function,  $\Psi$ , given by

$$\Psi = \| \mathbf{W}_\varepsilon [\mathbf{d} - f(\mathbf{m})] \|^2 + \alpha \| \mathbf{W}_s \mathbf{m} \|^2. \quad (4)$$

Here,  $\mathbf{d}$  is the data vector, given by

$$d_i = -\log R_i \quad i = 1, 2, \dots, N;$$

the parameters of the inversion,  $\mathbf{m}$ , are given by

$$m_j = \log \sigma_j \quad j = 1, 2, \dots, M;$$

$f(\mathbf{m})$  is the forward model for parameters  $\mathbf{m}$ ;  $\mathbf{W}_\varepsilon$  is an error weighting matrix;  $\mathbf{W}_s$  is a smoothness operator representing the discretized second derivative;  $\alpha$  is a regularization parameter which determines the amount of smoothing imposed on  $\mathbf{m}$  during the inversion.

[25] For the ERT forward problem, the soil column was partitioned into 14,720 triangular prisms (edge length  $\approx 6$  cm). For the inverse problem, in order to reduce

**Table 2.** Predefined Error Bounds for First ERT Data Filtering

	Lower Bound	Upper Bound
Injection current (mA)	2	100
Potential measurement (mV)	0	5000
Coefficient of variation of stacked potential measurements (%)	0	5

computational demands, we discretized the column into 3680 parameters. Thus, patches of 4 adjacent finite elements were lumped to one parameter, respectively (height  $\approx 6$  cm, horizontal edge length  $\approx 12$  cm).

[26] During the extraction of the soil column from the ground, the initially circular column cross section was deformed to a slightly ellipsoid shape with a maximal deviation of 2 cm with respect to a perfect circle. In a first approach, we used a perfectly cylindrical mesh to represent the column for the ERT inversion. In doing so, all horizontal cross sections of the ERT images exhibited a symmetrical feature which was aligned to the column wall deformation. This strongly suggests an artifact due to electrode and domain boundary misplacement. After we had implemented corrected electrode and column wall positions into the mesh, these features were reduced to a large extent. The corresponding changes in magnitude of the electrical conductivity were up to 50% (depending on the error level  $\varepsilon_{app}$ ). This finding stresses the importance of accurate implementation of the electrode and domain boundary positions into the inversion mesh.

[27] If  $\varepsilon_i$  is the measurement error in resistance  $R_i$  represented by the standard deviation, and if we assume that the measurement errors are uncorrelated, then  $\mathbf{W}_\varepsilon$  in (4) is a diagonal matrix defined as

$$\mathbf{W}_\varepsilon = \text{diag} \left[ \frac{R_1}{\varepsilon_1}, \frac{R_2}{\varepsilon_2}, \dots, \frac{R_N}{\varepsilon_N} \right]^T. \quad (5)$$

The inversion is stopped when the root-mean-square error  $\varepsilon_{RMS}$  reaches the target value of one. The root-mean-square error  $\varepsilon_{RMS}$  is given by

$$\varepsilon_{RMS} = \frac{1}{N} \sqrt{\sum_{i=1}^N W_{\varepsilon,i} (\mathbf{d}_i - f_i(\mathbf{m}))^2}. \quad (6)$$

From (6) and the objective function in (4) it is apparent that the smoothness inherent in the final ERT image is affected by the error estimates used to compute the data weighting matrix  $\mathbf{W}_\varepsilon$ .

[28] The true error  $\varepsilon$  comprises the measurement error as well as numerical (modeling) errors resulting from, for example, discretization errors or electrode positioning errors [LaBrecque et al., 1996; Zhou and Dahlin, 2003; Oldenborger et al., 2005]. In this study, we assumed that  $\varepsilon$  can be approximated using an absolute resistance error component,  $a_{app}$  ( $\Omega$ ), and a relative resistance error component,  $b_{app}$  (-), according to

$$\varepsilon_{app} = a_{app} + b_{app}R. \quad (7)$$

The optimal error weighting matrix  $\mathbf{W}_\varepsilon$  is related to the error level  $\varepsilon_{opt}$  which characterizes all noise in the system most accurately. An underestimation of  $\varepsilon$  leads to artifacts in the inversion results whereas its overestimation results in overly smooth ERT images [Binley et al., 1995; LaBrecque et al., 1996].

[29] The ERT inversion problem is ill conditioned, meaning that small errors in the data can lead to large errors (artifacts) in the results. In order to reduce the impact of noisy data on the ERT image we made use of a robust ERT inversion scheme as described by LaBrecque and Ward [1990]. Here, the error weighting matrix  $\mathbf{W}_\varepsilon$  is adapted for individual data points during each iteration (while the L2 norm is used to measure both model and data misfits). According to Morelli and LaBrecque [1996], reasonable results can be achieved with this approach even if the true error level is underestimated by 1 order of magnitude.

[30] However, even if using the robust inversion scheme, the inversion results still depend upon (1) the choice of the error level  $\varepsilon_{app}$  and (2) the criteria with which data points (e.g., outliers) are removed from the data set prior to inversion.

### 3.2.2. Data Error Analysis

[31] In ERT studies, data error has been typically appraised by either repeatability or reciprocity checks. The error estimate which results from the latter approach, here referred to as the reciprocal error  $\varepsilon_{N/R}$ , is empirically known to provide more useful values [e.g., LaBrecque et al., 1996]. However, as an estimate of the true error  $\varepsilon$ , the reciprocal error  $\varepsilon_{N/R}$  has substantial flaws. First, it is only a measure of precision and not accuracy. Additionally, it does not take into account correlations between the individual errors. Furthermore, it does not account for numerical errors. Hence, we subsequently used  $\varepsilon_{N/R}$  only as a starting and reference point for different parameterizations of error level  $\varepsilon_{app}$ . In order to reduce the degrees of freedom in this approach, we only consider uniform error level  $\varepsilon_{app}$  for all measurement configurations and time frames. Likewise, we neglect any correlation among the errors.

[32] Detailed information about how  $\varepsilon_{N/R}$  can be determined is reported by LaBrecque et al. [1996] and Slater et al. [2000]. Here, we present an approach which is an extension to the method proposed by LaBrecque et al. [1996].

[33] We first removed all obvious outliers from the ERT data set. This was done in two steps. First of all, all data that were outside predefined bounds of measured voltage, injection current, and coefficient of variation from stacking measurements [see Slater et al., 2000] were discarded. The bounds were chosen on the basis of empirical knowledge. They are listed in Table 2. Then, all data with a reciprocal error larger than 100% of the corresponding mean (of the normal and reciprocal) transfer resistance  $R_{N/R}$  were removed. After this, 17,000 to 20,000 of the initial 23,130 normal and reciprocal data were retained for each frame.

[34] In the next stage we subdivided the range of measured transfer resistances into logarithmically equally sized bins. For each bin, the standard deviation  $s_{bin}$  of the reciprocal errors was calculated. The error model parameters  $a_{N/R}$  and  $b_{N/R}$  were determined by fitting the right-hand side of (8) to  $s_{bin}$  (Figure 2). The fitted parameters  $a_{N/R}$

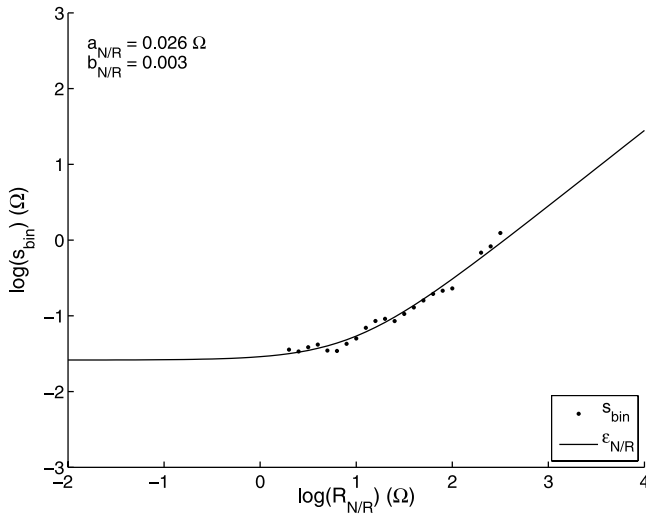


**Figure 2.** The standard deviation  $s_{bin}$  of the  $N/R$  misfits which were collected in bins and the corresponding error model fit  $\varepsilon_{N/R}$  for the first of the 48 ERT frames. The error model parameters  $a_{N/R}$  and  $b_{N/R}$  are shown at the top left.

and  $b_{N/R}$  define the error  $\varepsilon_{N/R}$  which represents the standard deviation of the reciprocity error:

$$\varepsilon_{N/R} = a_{N/R} + b_{N/R}R_{N/R}. \quad (8)$$

Following this approach, we found that  $\varepsilon_{N/R}$  decreased with progression of the tracer front (Figure 3). An explanation for this behavior is that the increased solute concentration enhanced the electrode to soil contact. From this it follows that  $\varepsilon_{N/R}$  is spatially variable, not only because of varying solute concentration but also because of spatially varying water content. Indeed, we could confirm this when applying the normal-reciprocal ( $N/R$ ) error analysis to subsets of the ERT data. Additionally, we could observe an increase of  $\varepsilon_{N/R}$  when the tracer front was passing the location of the corresponding data subset. We attribute this to the temporal aliasing which occurred because of the time gap between normal and reciprocal measurements. (The time gap was not fixed for the individual electrode configurations and varied between some minutes up to 8 h.) However, in a first approach, we restrict ourselves in investigating the spatially and temporally mean  $\varepsilon_{N/R}$  only (i.e., in the following,  $\varepsilon_{N/R}$  always denotes the spatially and temporally mean  $\varepsilon_{N/R}$ ). The mean of the error model parameter  $a_{N/R}$  was found to be  $0.009 \Omega$  (maximum  $0.031 \Omega$ ) whereas the mean of parameter  $b_{N/R}$  was  $0.005\%$  (maximum  $0.011\%$ ).

### 3.2.3. Data Selection

[35] The mean transfer resistances  $R_{N/R}$  of all electrode configurations of an individual time frame are referred to as data points in the following. When a time series of individual ERT frames has to be inverted, it is desirable to (1) invert identical data points for each individual frame in order to yield similar sensitivity distributions for each frame, (2) invert data points which are distributed as uniformly as possible over the inversion domain, and (3) reduce the number of data points in order to decrease the computational demand.

[36] In the following we used  $\varepsilon_{N/R}$  to meet the first criteria. Data points which had a  $N/R$  misfit larger than the fivefold of  $\varepsilon_{N/R}$  in at least one of the 48 frames were removed for the entire time series. With this approach, the number of retained data points was 6,371, covering the whole inversion domain. We are aware that the choice of the threshold is largely arbitrary. Furthermore, a constant threshold leads to a bias in the spatial data point density when regions with varying electrode contact are present, e.g., because of spatial water content variations. Spatially varying thresholds with respect to the electrode contact could be used to obtain a uniform data point distribution. For sake of simplicity we refrain from refined data selection approaches in this study. Instead, we focus on comparing inversion results of different error levels  $\varepsilon_{app}$ . The investigated  $\varepsilon_{app}$  were chosen with respect to the reciprocal error  $\varepsilon_{N/R}$ .

### 3.3. Relating Electrical Conductivity to Solute Concentration

[37] The soil bulk electrical conductivity is assumed to be related to the solute electrical conductivity  $\sigma_w$  ( $\mu\text{S}/\text{cm}$ ) according to the model of *Waxman and Smits* [1968]:

$$\sigma_b = \frac{1}{F}\sigma_w + \sigma_s, \quad (9)$$

where  $\sigma_s$  ( $\mu\text{S}/\text{cm}$ ) is the ohmic surface conductivity of the soil solid phase (largely related to the clay content in the soil) and  $F$  (-) is the so-called formation factor. Following Archie's law [Archie, 1942], the formation factor  $F$  accounts for pore space characteristics. For simplicity, we here also incorporate the saturation dependence of the electrolytic conductivity component in (9) (according to Archie's "second equation") into the formation factor, which then can be written as

$$F = \omega\Phi^{-m} \left( \frac{\theta}{\Phi} \right)^{-n}, \quad (10)$$

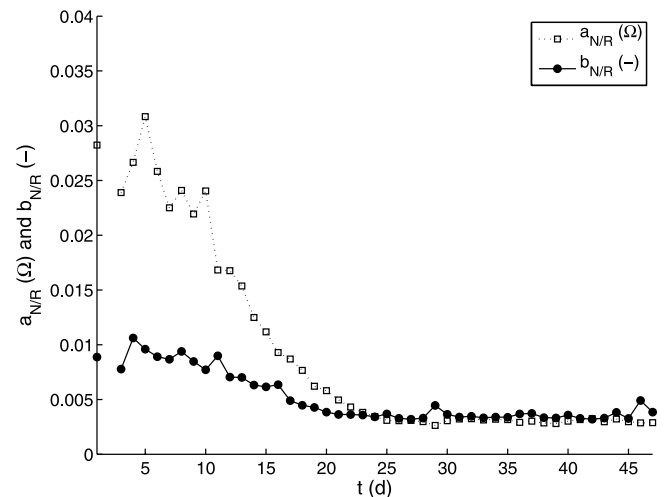


**Figure 3.** Time series of  $N/R$  error model parameters found during the experiment.

where  $\Phi$  is the porosity,  $\theta$  the water content, and  $\omega$ ,  $m$ , and  $n$  are empirical (fitting) parameters.

[38] In order to relate bulk electrical conductivity to solute concentration, five assumptions are made.

[39] 1. First, we assume that under hydraulic steady state conditions the formation factor (here including the water content influence) was spatially variable but remained temporally constant. Knowledge of the actual porosity, the water saturation, and the formation and saturation exponents is not needed.

[40] 2. In the second assumption we presume that the ohmic mineral surface conductivity remained approximately constant during the course of our experiment, i.e., was in a first approximation independent of salinity. There is evidence in literature that this assumption is justified [e.g., *Revil and Glover, 1998*] in the regime of our experiment.

[41] 3. In order to apply the approach, we have to know the solute concentration in the soil water for the entire soil column for two distinct salinity states. Hence, the third assumption is that the solute concentration in the soil water was spatially constant after the solute concentration in the effluent had reached stable values.

[42] If the three assumptions are valid, the solute electrical conductivity  $\sigma_w$  is spatially constant at two salinity states: state 1 at the start of the experiment when  $\sigma_w$  corresponded to tap water (503  $\mu\text{S}/\text{cm}$ ) and state 2 at the end of the experiment when  $\sigma_w$  corresponded to  $\text{CaCl}_2$  solution (2,530  $\mu\text{S}/\text{cm}$ ).

[43] On the basis of the first three assumptions we can derive the electrical conductivity of the solute at an arbitrary state  $t$  from the bulk electrical conductivity at state 1 and state 2. First, we set up (9) for all three solute saturation states and obtain

$$\sigma_{b,t} = \frac{1}{F} \sigma_{w,t} + \sigma_{s,t} \quad (11a)$$

$$\sigma_{b,1} = \frac{1}{F} \sigma_{w,1} + \sigma_{s,1} \quad (11b)$$

$$\sigma_{b,2} = \frac{1}{F} \sigma_{w,2} + \sigma_{s,2}. \quad (11c)$$

Next, we subtract (11b) from (11a) and (11c), respectively. This yields

$$\sigma_{b,t} - \sigma_{b,1} = \frac{1}{F} \sigma_{w,t} - \frac{1}{F} \sigma_{w,1} \quad (12a)$$

$$\sigma_{b,2} - \sigma_{b,1} = \frac{1}{F} \sigma_{w,2} - \frac{1}{F} \sigma_{w,1}. \quad (12b)$$

The mineral surface conductivity is canceled out.

[44] In a last step, we divide (12a) by (12b) which results in

$$\frac{\sigma_{w,t} - \sigma_{w,1}}{\sigma_{w,2} - \sigma_{w,1}} = \frac{\sigma_{b,t} - \sigma_{b,1}}{\sigma_{b,2} - \sigma_{b,1}}. \quad (13)$$

The impact of the formation factor is, thus, canceled out as well.

[45] Two further assumptions are used to relate bulk electrical conductivity to solute concentration  $C$  (assumptions 4 and 5).

[46] 4. We assume that the ratio between relative changes of chloride concentration  $(C_t - C_1)/(C_2 - C_1)$  and solute electrical conductivity  $(\sigma_{w,t} - \sigma_{w,1})/(\sigma_{w,2} - \sigma_{w,1})$  was constant over time.

[47] 5. We assume that the latter ratio was constant for the entire soil column and could be obtained from the effluent BTC.

[48] Here,  $C_t$  is the chloride concentration for time  $t$ ,  $C_1$  is the chloride concentration at salinity state 1 (54 mg/L) and,  $C_2$  is the chloride concentration at salinity state 2 (642 mg/L).

[49] The corresponding function, here denoted as  $g$ , was determined by relating the chloride content in the effluent with the corresponding electrical conductivity measurements:

$$\frac{(C_t - C_1)}{(C_2 - C_1)} = g \left( \frac{\sigma_{w,t} - \sigma_{w,1}}{\sigma_{w,2} - \sigma_{w,1}} \right). \quad (14)$$

(14) can be resolved to chloride concentration at time  $t$ ,  $C_t$ :

$$C_t = g \left( \frac{\sigma_{w,t} - \sigma_{w,1}}{\sigma_{w,2} - \sigma_{w,1}} \right) (C_2 - C_1) + C_1. \quad (15)$$

All measured electrical conductivities were corrected for temperature using the relationship published by *Franson [1985]*. Although the environment of the laboratory was temperature controlled, temperature shifts up to a magnitude of  $\pm 4^\circ\text{C}$  occurred because of malfunctions of the climate control and impacts of outside temperature variations over the duration of the experiments (15 November 2005 to 1 January 2006).

[50] We observed that the electrical conductivity  $\sigma_w$  of the effluent (maximum: 440  $\mu\text{S}/\text{cm}$ ) did not reach that of the irrigation water (503  $\mu\text{S}/\text{cm}$ ). Again, after the soil water ionic content in the effluent was in equilibrium with the tracer irrigation water, the electrical conductivity of the effluent was lower than the one of the irrigation water (2,450  $\mu\text{S}/\text{cm}$  compared to 2,530  $\mu\text{S}/\text{cm}$ ). Both times, the balance of  $\text{Ca}^{2+}$  concentration between irrigation water and effluent is negative. A probable explanation for the decrease in salinity is hence calcium carbonate precipitation together with degassing of carbon dioxide. We are aware that this violates our assumptions made for the calibration of the petrophysical model. However, for sake of simplicity, we ignore this fact and assume a closed solute electrical conductivity balance at this point (constant 440  $\mu\text{S}/\text{cm}$  and constant 2,450  $\mu\text{S}/\text{cm}$  for the first and last frame, respectively).

[51] An analysis of irrigation and outflow water showed that the mass of applied chloride was conserved during the experiment (mass balance: 98.3%). Analyzing the effluent, we found that the function  $g$  in (15) between change in solute electrical conductivity and change in chloride concentration was not linear but exponential. We fitted a second-order polynomial to the data in order to relate solute electrical conductivity to chloride concentration.

[52] Subsequently, we used (13) and (15) to derive (1) the breakthrough curve of the flux-averaged chloride concen-

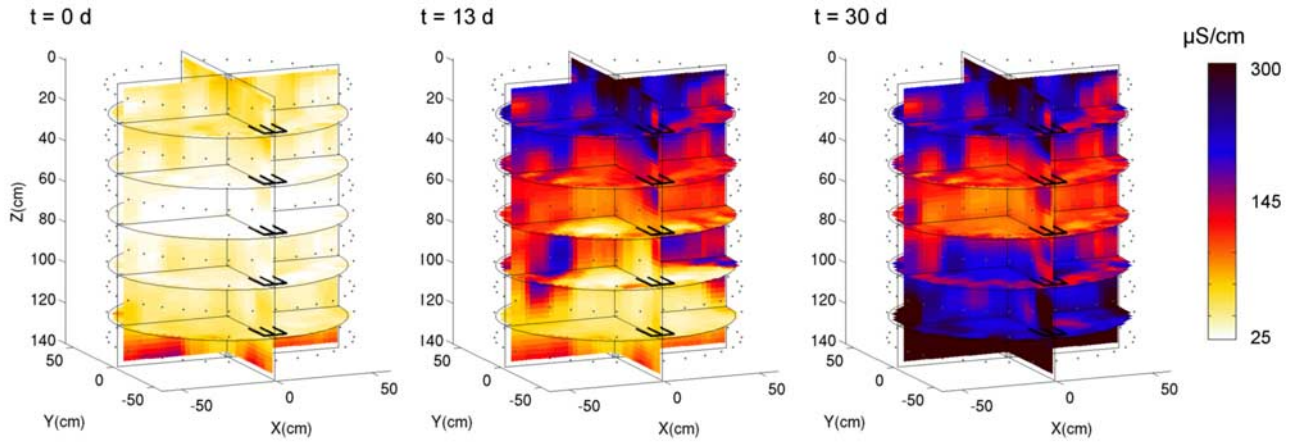


**Figure 4.** The 3-D ERT bulk electrical conductivity at  $t = 0$  d,  $t = 13$  d, and  $t = 30$  d for  $a_{app} = 0.02 \Omega$  and  $b_{app} = 0.01$  ( $\varepsilon_{app} \approx 2\varepsilon_{N/R}$ ).

tration in the effluent, (2) the breakthrough curves of the resident chloride concentration sampled with each TDR probe, and (3) the breakthrough curves of the resident chloride concentration for each ERT voxel. The scaling was performed for each TDR probe and each ERT voxel and the effluent data individually by means of the bulk electrical conductivities  $\sigma_{b,1}$  and  $\sigma_{b,2}$  which were measured at the corresponding probe/voxel as well as the effluent data.

### 3.4. Comparing ERT Data to TDR and Effluent Data

[53] With an estimated accuracy of approximately 1% [Huisman *et al.*, 2008] and a measured precision of approximately 1%, we consider TDR as appropriate to rate the validity of the electrical conductivity data which were obtained with ERT. The sampling volume of a three-rod TDR probe is sensitive to the rod spacing to rod diameter ratio which is in our study 10:1. According to Ferré *et al.* [1998], the sampling volume of our probes can be approximated by a cylinder around the central rod with a radius of one and a half time the rod spacing and length of the rods (approximately 800 cm<sup>3</sup>). It should be noted that the sensitivity is strongly biased toward the vicinity of the rods.

[54] The volume of one ERT voxel is approximately 90 cm<sup>3</sup>, whereas the voxel size should not be confused with the ERT resolution. In order to compare ERT and TDR data, we related the mean of the ERT electrical conductivity of all voxels intersecting the TDR sampling volume to the corresponding TDR probe.

[55] We compare the TDR- and ERT-derived BTCs by means of apparent CDE parameters, the apparent velocity  $v_a$  (cm/d) and the apparent dispersivity  $\lambda_a$  (cm):

$$\frac{dC}{dt} + v_a \frac{dC}{dx} - \lambda_a v_a \frac{d^2C}{dx^2} = 0. \quad (16)$$

Here, we fit the solution of the third type boundary value problem for a step input and for resident concentrations to the BTCs [Parker and van Genuchten, 1984]. The apparent CDE velocity  $v_a$  and the apparent CDE dispersivity  $\lambda_a$  are not related to a physical process. Similar to temporal moments they merely capture the main characteristics of the

breakthrough curve in a condensed manner [see, e.g., Vanderborght *et al.*, 2001]. We use the apparent CDE parameters since they provide better means to compare breakthrough curve data from different depths and flow rates. Temporal moments always change with depth and flow rate whereas for a homogeneous transport process, the apparent CDE parameters should remain constant with depth and the dispersivity with flow rate. Changes of these parameters with depth and flow rate directly indicate heterogeneous transport.

[56] The flux concentrations measured in the effluent of the column were fitted using the solution of the CDE for a first-type boundary condition. By means of the apparent CDE parameters, we were able to quantitatively compare the breakthrough curve of the mean resident chloride concentrations of the bottommost ERT voxels with the one of the flux concentration which was measured in the effluent. This provided an additional evaluation of the quantitative interpretability of the ERT images.

[57] The residuals between TDR- and ERT-derived apparent velocity  $Rd_v$  and apparent dispersivity  $Rd_\lambda$  were calculated according to

$$Rd_v = \frac{v_{a,(ERT)} - v_{a,TDR}}{v_{a,TDR}} \cdot 100 \quad (17)$$

and

$$Rd_\lambda = \frac{\lambda_{a,(ERT)} - \lambda_{a,TDR}}{\lambda_{a,TDR}} \cdot 100 \quad (18)$$

Likewise, the residuals between the apparent CDE parameters for the effluent BTC and the averaged BTC of the bottommost ERT voxels were calculated.

## 4. Results and Discussion

### 4.1. ERT Bulk Electrical Conductivity Images

[58] The three-dimensional variation in bulk electrical conductivity,  $\sigma_b$ , for day 0, day 13, and day 30 is shown in Figure 4. The corresponding error model parameters were  $a_{app} = 0.02 \Omega$  and  $b_{app} = 0.01$ . The left-hand side of Figure 4

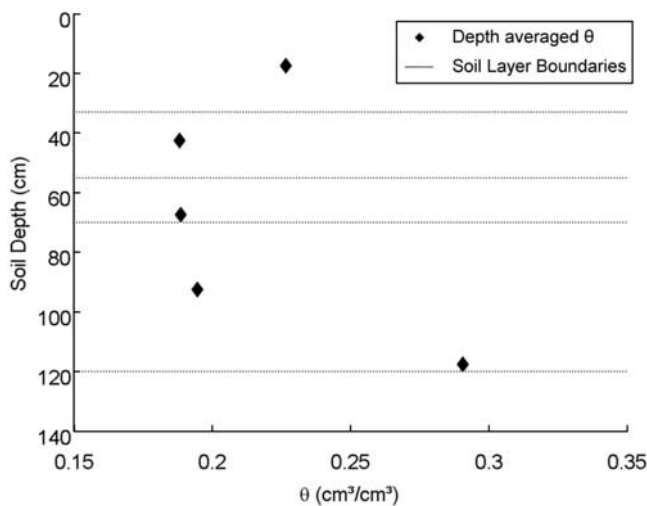


**Figure 5.** The water content profile inside the soil column measured with TDR.

(day 0) depicts the initial state where the soil water composition corresponded to tap water composition. The right-hand side of Figure 4 (day 30) depicts the final state where the composition of soil water corresponded to the  $\text{CaCl}_2$  solution. Therefore, the bulk electrical conductivity of day 0 and day 30 provide explicit information on the water content distribution inside the lysimeter. The distribution is (qualitatively) in accordance with the TDR-derived water content (Figure 5).

[59] The image shown in the central position in Figure 4 (day 14) corresponds to a day when the tracer front had reached the bottommost third of the column. It can be seen that the tracer front cannot be delineated from a single bulk electrical conductivity image alone.

#### 4.2. Comparison of ERT- and TDR-Derived Bulk Electrical Conductivity

[60] Figure 6 shows the BTCs obtained from TDR and the corresponding ERT-derived voxel BTCs at a depth of 42.5 cm. The impact of the different  $\varepsilon_{app}$  on the ERT bulk electrical conductivity can be seen. For  $\varepsilon_{app} \ll \varepsilon_{N/R}$  (Figure 6, top), the voxel BTCs and the corresponding mean BTC are noisy, whereas for  $\varepsilon_{app} \gg \varepsilon_{N/R}$  (Figure 6, bottom), the BTCs are smooth. For this error level of 42.5 cm, the ERT image-derived electrical conductivity was consistently greater than the one captured with TDR. When  $\varepsilon_{app}$  is slightly higher than  $\varepsilon_{N/R}$ , the mean voxel BTC matches the TDR data best. As an example, the response with  $\varepsilon_{app} \approx 2\varepsilon_{N/R}$  is shown in Figure 6 (middle).

[61] Figure 7 shows vertical bulk electrical conductivity profiles at the two TDR transects at day 31. By this time, the  $\text{CaCl}_2$  solution had replaced all the tap water in the soil and, thus, the observed spatial variability in electrical conductivity is attributed to spatial variations in water content and clay content rather than solute concentration. Instead they are caused by spatial variations in water content and clay content. If we infer from the layering of the soil that the horizontal gradients in water content and clay content are negligible as compared to the vertical gradients, we can explain the systematic deviations between the smooth ERT

images and TDR at an individual soil depth, e.g., at depth 42.5 cm (see Figure 6, bottom, and Figure 7).

[62] The locations of the peaks in the electrical conductivity profile of the inversion with  $\varepsilon_{app} \ll \varepsilon_{N/R}$  and  $\varepsilon_{app} \approx 2\varepsilon_{N/R}$  in Figure 7 correspond to the depths of the horizontal electrode rings. The troughs correspond to the interring positions where the TDR probes are located. It is unlikely that this artifact-like feature is related to the metal rods of the TDR probes as the metal rods would result in an increase of electrical conductivity. The feature resembles rather an artifact due to an underestimation of the optimal error level: it becomes less associated with the ERT sensitivity distribution as well as less pronounced with larger  $\varepsilon_{app}$ .

[63] As discussed above, the mismatch between ERT and TDR is largely dependent on the error level  $\varepsilon_{app}$  used in the ERT inversion. Apart from this there may have been other contributing factors. First, the different sampling volumes of TDR and ERT could have led to a mismatch, especially if there were large heterogeneities in bulk electrical conductivity at the TDR measurement scale. A mismatch could have also been caused by errors in the TDR and/or ERT data. Systematic and random errors in the TDR-derived electrical conductivity may have been originated from alterations of the pore space or alterations of the rod spacing during the probe installation [Huisman *et al.*, 2008]. However, detailed studies similar to those presented by Rothe *et al.* [1997], who investigated the effect of soil compaction on the TDR-derived dielectric constant, are presently not available. For ERT, systematic and random errors in the ERT data could have been caused by, e.g., electrode misplacement. As discussed, we could reduce the misfit between ERT and TDR results significantly by implementing the correct electrode position in the finite element ERT mesh. Furthermore, we expect further improvement with a finer ERT mesh discretization. In this study, we abstained from this because of computational limitations. Finally, the TDR steel rods could have caused artifacts because of the large electrical conductivity contrast which the TDR rods provide themselves. However, artifact-like features in the vicinity of the TDR probes were visually not observed or did not exceed the range of the bulk electrical conductivity variations in the corresponding cross section. Therefore, we consider that the effect of the TDR rods on the ERT images is of minor importance. Further investigations of these issues is warranted but exceed the scope of this study.

#### 4.3. Overshooting Values in the ERT Image Series

[64] For some voxels, the ERT inversion occasionally produced overshooting values (Figure 6); that is, the calculated bulk electrical conductivity values were larger than the ones found when the soil water was in chemical equilibrium with the tracer solution. Such a behavior was not observed in the data from the TDR probes. The overshooting values are likely to be related to ERT imaging artifacts. Note that the overshooting values are only observable relative to the ERT-derived bulk electrical conductivity after chemical equilibrium with the tracer had been reached. It can either represent overestimation at the time of the overshoot or underestimation at the time of chemical equilibrium. We suspect that the artifacts reflect how the ERT regularization acts on the reconstructed image for different electrical

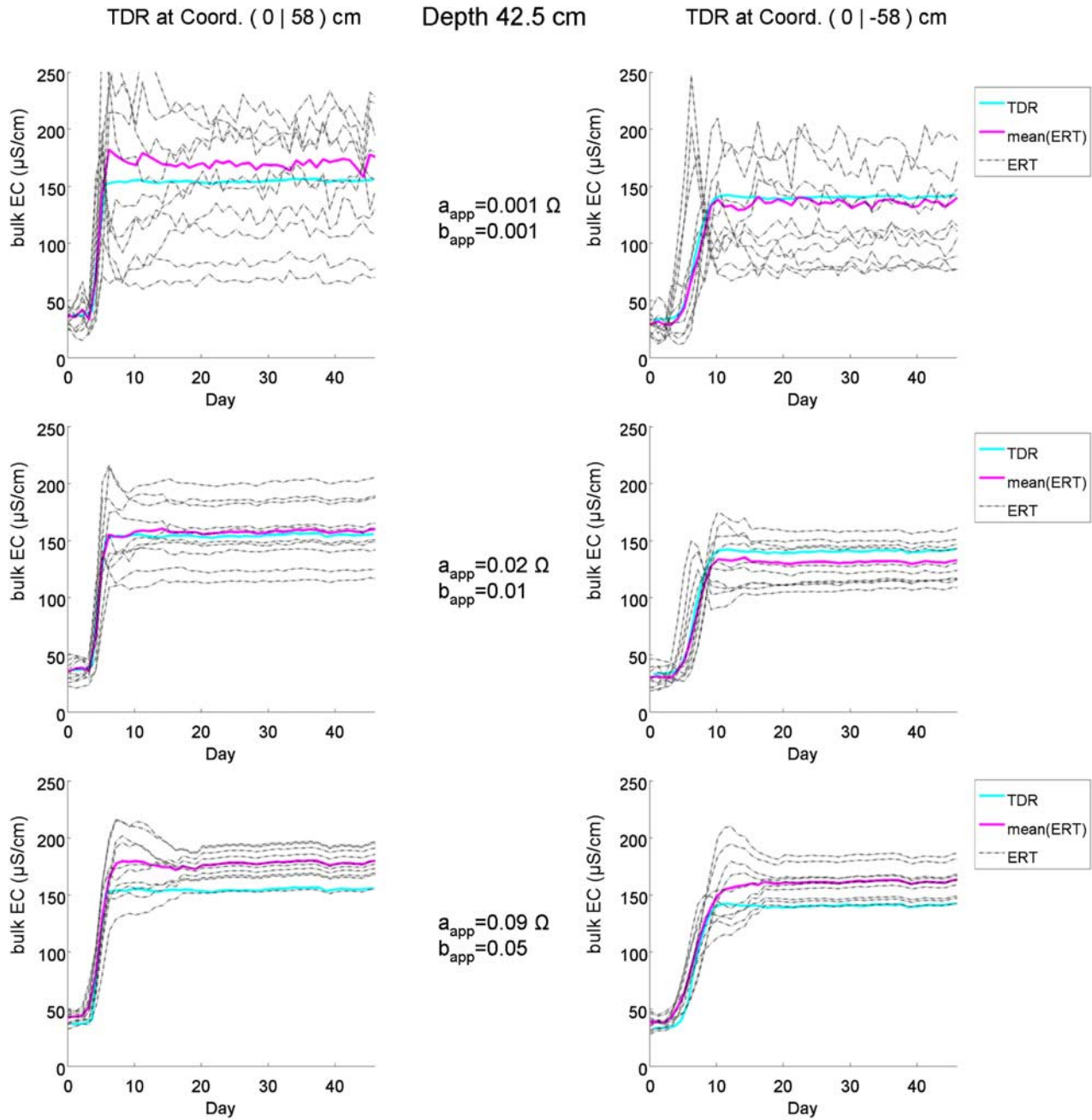


**Figure 6.** TDR bulk electrical conductivity (EC) BTCs at depth 42.5 cm compared to the mean ERT voxel BTC in the vicinity of the corresponding TDR probe locations. Additionally, the corresponding individual voxel BTCs are depicted. The impact of the ERT inversion error level on the results is shown for three examples: (top)  $\varepsilon_{app} \ll \varepsilon_{N/R}$ , (middle)  $\varepsilon_{app} \approx 2\varepsilon_{N/R}$ , and (bottom)  $\varepsilon_{app} \gg \varepsilon_{N/R}$ .

conductivity gradients. When visually inspecting the location of the overshooting values we could not find any systematics connected to their occurrence.

#### 4.4. Chloride Concentration Images

[65] From Figure 8, in which the ERT-derived chloride concentrations for  $a_{app} = 0.02 \Omega$  and  $b_{app} = 0.01$  are shown, it can be seen that the tracer front is clearly resolved. The maximal gap between the most advanced and most delayed part of the tracer front during the experiment was approximately 50 cm (see Figure 8, day 14). Note that the

smoothness constraint in the ERT inversion results in a smooth image of the real tracer front progression. In addition, the spatial resolution is worse and smoothing is more pronounced in the center of the column where the sensitivity is lower than near the column's perimeter where the electrodes are located.

#### 4.5. Comparison of ERT- and TDR-Derived Chloride Concentration

[66] In Figure 9, the chloride concentration BTCs for TDR and the mean of the neighboring ERT voxels at depth

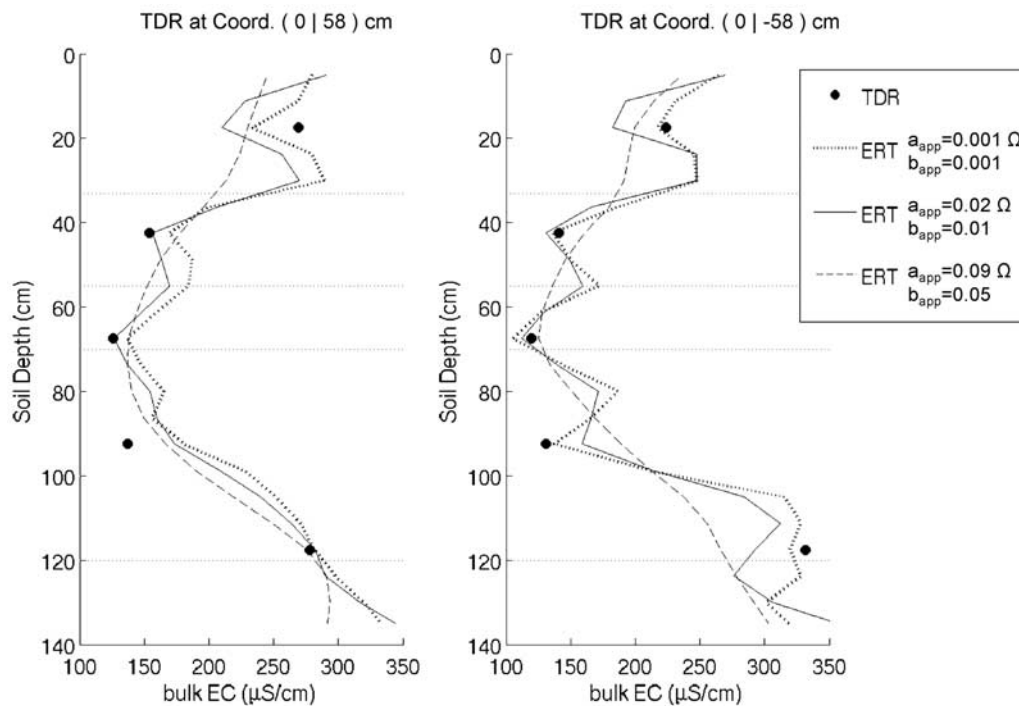


**Figure 7.** The vertical bulk electrical conductivity profile along the two TDR transects. Next to the TDR data, ERT image data for three different error levels are shown. The ERT data correspond to the moving average of ERT voxels intersecting an equivalent of the support volume of TDR.

42.5 cm are shown. For  $\varepsilon_{app} \ll \varepsilon_{N/R}$  (Figure 9, top), the BTCs were noisy; for  $\varepsilon_{app} \gg \varepsilon_{N/R}$  (Figure 9, bottom), the ERT response did not exceed the TDR response. However, the dispersion of the tracer front is larger when measured with ERT data than when based on TDR data. Again, the midsection of Figure 9 depicts  $\varepsilon_{app} \approx 2\varepsilon_{N/R}$ . Here, a good match between TDR and mean voxel ERT BTCs can be observed.

#### 4.6. Comparison of Apparent CDE Parameters From ERT and TDR Chloride BTCs

[67] Figure 10 shows the apparent velocities of TDR and mean voxel ERT BTCs. It shows that the solute was traveling faster at the TDR probes at the XY coordinates (0 | 58) than at the XY coordinates (0 | -58). It can be seen that the apparent velocity is relatively insensitive to  $\varepsilon_{app}$ . Using  $\varepsilon_{app} \approx 4\varepsilon_{N/R}$  results in the best match between ERT and TDR (Table 3). For this ERT error level, the mean residual is below 0.1% (standard deviation 1.6%). Note that the residuals listed in Table 3 are valid only for regions with similar ERT sensitivity as the one at the TDR locations. The accuracy of ERT is expected to worsen with increasing distance to the column walls.

[68] The ERT-derived apparent dispersivities, in contrast, are strongly dependent on the choice of  $\varepsilon_{app}$  (Figure 11). This is also apparent from visual inspection of the BTCs (Figure 9). For  $\varepsilon_{app} \approx \varepsilon_{N/R}$ , the apparent dispersivities are, on average, overestimated by 17.5% (Table 3). The highest precision was obtained for  $\varepsilon_{app} \approx 2\varepsilon_{N/R}$  (standard deviation of the residuals 26.8%).

[69] The overestimation of the apparent dispersivities can be explained by the effect of the smoothness constraint in the ERT inversion [Kemna *et al.*, 2002; Vanderborght *et al.*,

2005]. Additionally, as the solute moved approximately 3 cm on average during one ERT snapshot, temporal smearing is expected to support an overestimation of apparent dispersivities [Slater *et al.*, 2002; Vanderborght *et al.*, 2005].

[70] Like the apparent velocities, the dispersivities differ in magnitude between the two TDR transects at the XY coordinates (0|58) and (0|-58). For the error levels  $\varepsilon_{app} \approx \varepsilon_{N/R}$  and  $\varepsilon_{app} \approx 2\varepsilon_{N/R}$  the difference in magnitude is recovered by ERT. For these error levels, the shapes of the dispersivity depth profiles are recovered best if both transects are considered.

[71] The ERT image-derived apparent velocities are estimated well regardless of the choice of  $\varepsilon_{app}$ , whereas for a good estimation of the apparent dispersivities the error level  $\varepsilon_{app}$  is important. This suggests that investigations on the optimal error level  $\varepsilon_{app}$  can be undertaken by means of the misfit between TDR- and ERT-derived apparent dispersivities.

#### 4.7. Comparison of Apparent CDE Parameters From ERT and Effluent Chloride BTCs

[72] The 1-D apparent velocity determined from the effluent data and the one derived from the mean of all BTCs in the bottommost ERT voxels match almost perfectly (Table 4). Except for overly smooth inversions ( $\varepsilon_{app} \gg \varepsilon_{N/R}$ ), the misfit is less than 2% with respect to the effluent data (Table 4).

[73] The good match in 1-D apparent velocity suggests that the ERT chloride BTCs recovered the bulk chloride mass correctly, at least at the bottom of the column. We draw this conclusion as the integral over the effluent BTC and the integral over 1-D ERT BTC at the bottom of the column yield an identical mass. This is supported by the fact

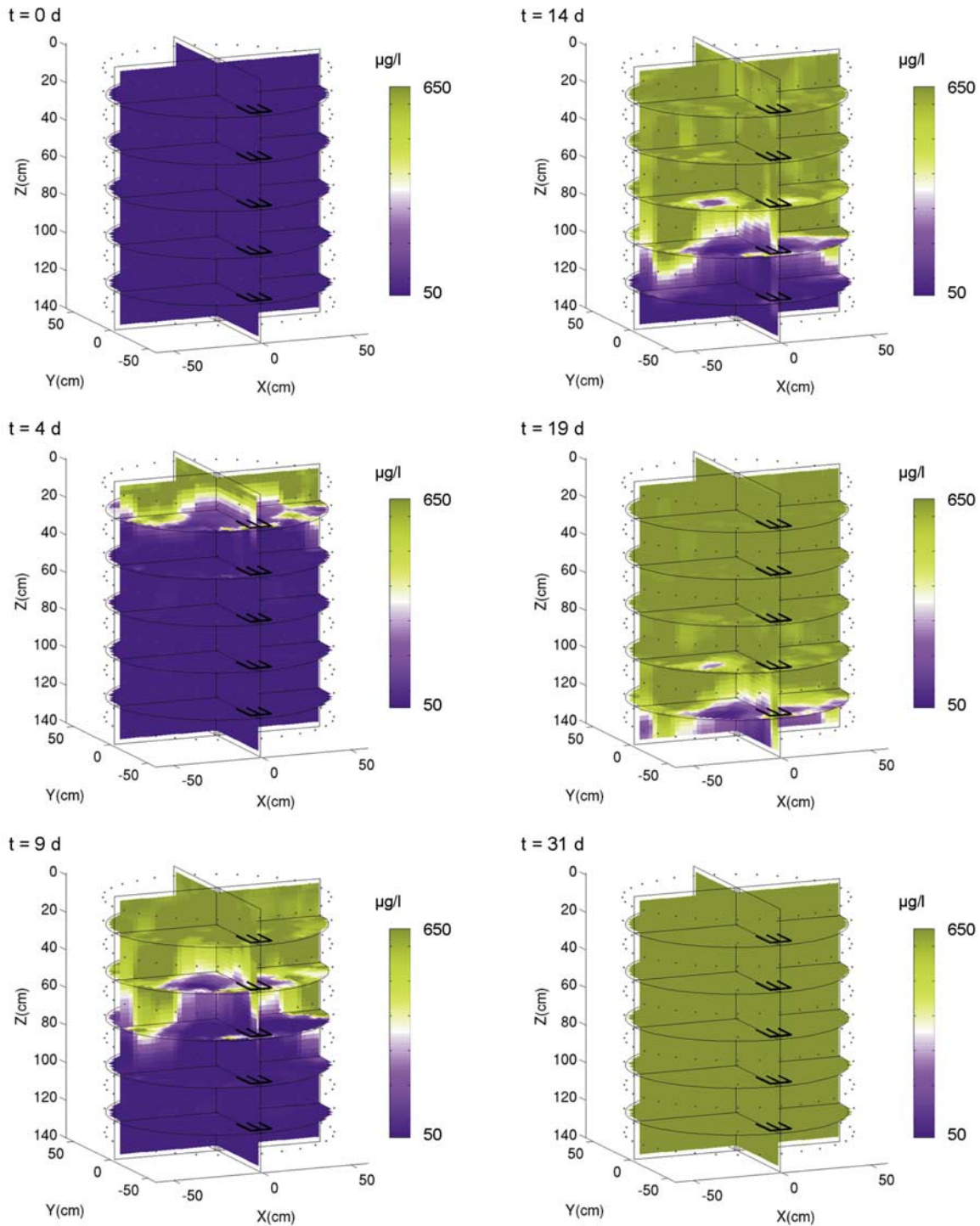


**Figure 8.** The 3-D tracer front progression shown in chloride concentration for  $a_{app} = 0.02 \Omega$  and  $b_{app} = 0.01$  ( $\varepsilon_{app} \approx 2\varepsilon_{NR}$ ).

that we scaled the ERT voxel BTCs to the correct minimum and maximum chloride concentrations.

[74] The deviations between the ERT- and effluent-derived apparent dispersivities are in the range of the ones we observed in the comparison with the TDR data (4% for  $\varepsilon_{app} \gg \varepsilon_{NR}$  to 31% for  $\varepsilon_{app} \approx 2\varepsilon_{NR}$ ). The ERT-derived dispersivity is exclusively smaller than the dispersivity

found in the effluent BTC. The opposite would be expected because of the smoothness constraint in the ERT inversion.

[75] A possible explanation is that boundary effects and decreased sensitivity lead to artifacts in the bottommost ERT voxels as they were located outside the electrode array. Apart from this, the water collection system at the outlet of

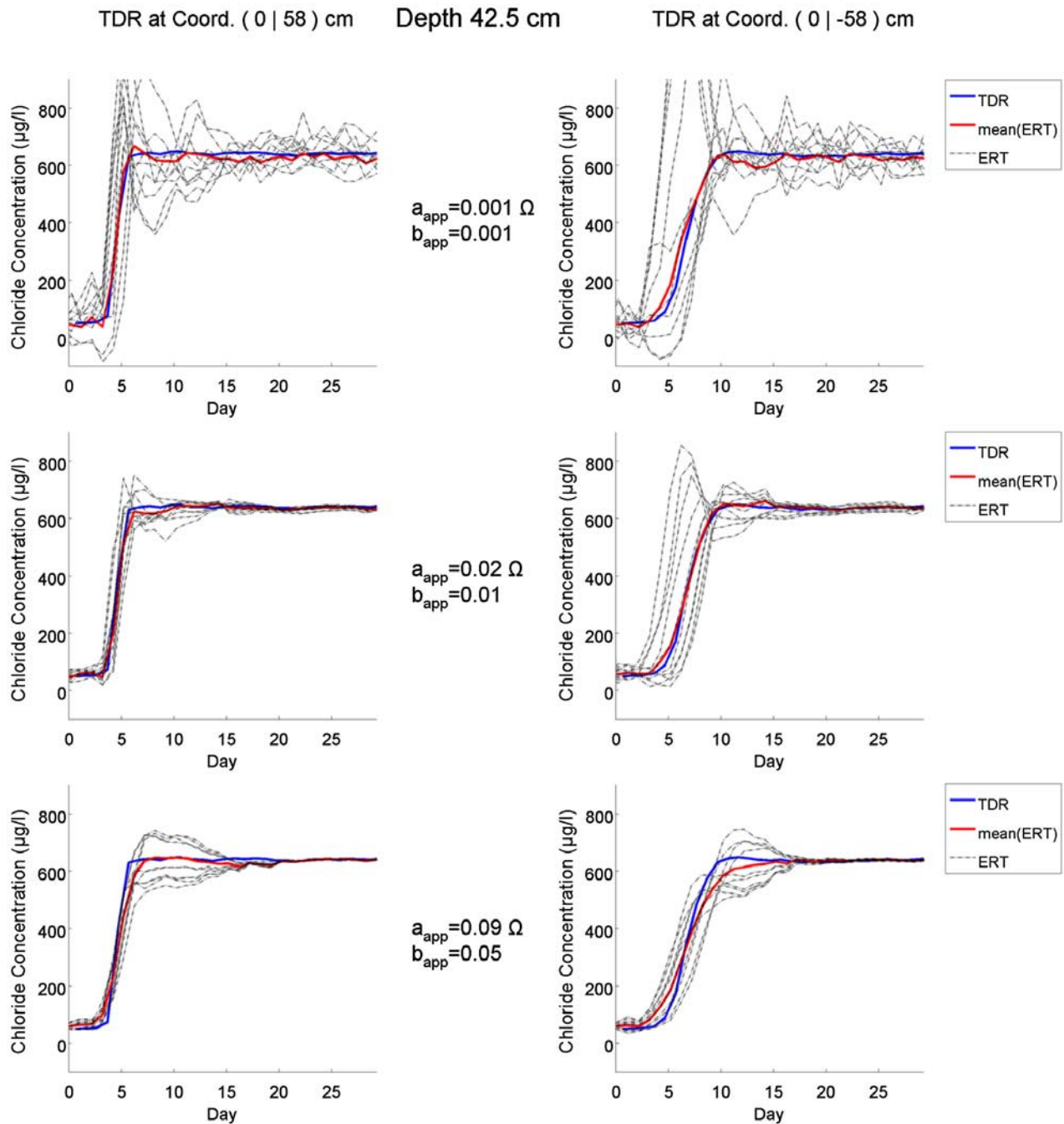


**Figure 9.** TDR chloride concentration BTCs at depth 42.5 cm compared with the mean ERT voxel BTC in the vicinity of the corresponding TDR probe locations. Additionally, the corresponding individual voxel BTCs are depicted. The impact of the ERT inversion error level on the results is shown for three examples: (top)  $\varepsilon_{app} \ll \varepsilon_{N/R}$ , (middle)  $\varepsilon_{app} \approx 2\varepsilon_{N/R}$ , and (bottom)  $\varepsilon_{app} \gg \varepsilon_{N/R}$ .

the column might have generated additional dispersion to the effluent BTC.

[76] An alternative intuitive explanation of why the ERT-derived dispersivity overestimates the TDR-derived one but underestimates the dispersivity in the effluent BTC is depicted in Figure 12. In Figure 12 a schematic of the tracer transport inside the soil column conceptualized with stream tubes is shown for illustration purpose. Within each stream tube (local scale), the tracer is transported with different velocity. At each local-scale tracer front, a BTC

is shown which represents the local-scale dispersivity. At the local scale, the smoothness-constrained ERT recovers the travel depth correctly (and hence the transport velocity) but overestimates the dispersivity (dashed line). This is what we observed when comparing TDR- and ERT-derived BTCs and what was also found by *Vanderborght et al.* [2005]. At the column scale, the smoothness-constrained ERT is expected to underestimate the travel depth variability and hence the stream tube velocity variability (dotted line). The stream tube velocity variability, however, is positively

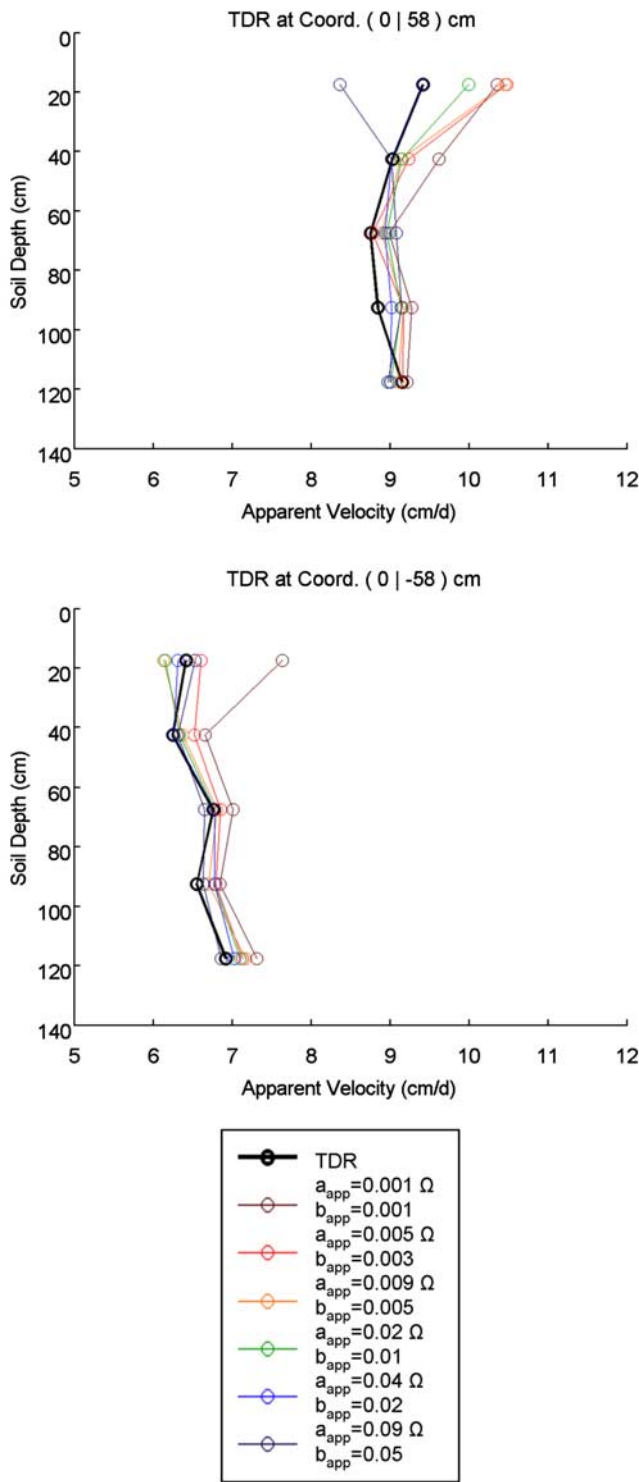


**Figure 10.** Apparent velocities  $v_a$  (cm/d) from TDR and the corresponding mean of the ERT voxel BTCs as a function of  $\epsilon_{app}$ .

correlated with a dispersivity component which is generated above the local scale [e.g., Jury and Roth, 1990]. This dispersivity component would be underestimated. If in our case this is the dominant contribution to the column-scale dispersivity, this would explain why ERT underestimated the latter. Theoretically, this hypothesis could be investi-

gated by means of TDR. However, in our study this was not possible as the TDR probes sampled only regions with similar and high ERT sensitivity.

### 5. Summary and Conclusion

[77] We have presented a detailed study on some basic issues in the general application of ERT to quantify solute transport parameters in unsaturated undisturbed soils. The experimental setup which we used in this study allowed us to directly translate bulk electrical conductivity to solute concentration without a priori knowledge of the petrophysical properties of the soil material. A drawback of the approach is that it is only applicable when the following conditions are met: (1) hydraulic steady state conditions exist, and (2) no spatial variation of the soil water solute concentration exists for at least two solute saturation states in the entire domain of the column. Applications of the approach at the field scale are possible; however, large efforts would be needed to meet the prerequisites (e.g., large amount of water and time). This renders the approach more appropriate for laboratory column-scale studies.

[78] We did not observe mass balance problems when using ERT, as reported by, e.g., Singha and Gorelick [2005]. We suspect that this is connected with (1) the application of the tracer as a step which is homogeneously distributed over the entire upper boundary of the investigated domain, (2) the location of the electrodes at the vertical boundaries of the investigated domain, (3) the improved sensitivity of ERT within a bounded domain, and (4) the scaling of the bulk electrical conductivity to the minimum and maximum chloride concentration.

[79] We introduced an improved method to quantitatively characterize the noise in the raw ERT data by means of normal and reciprocal measurements. The method is based on the approach of LaBrecque et al. [1996]. In our revised approach, noise in the complete range of transfer resistances is sampled (a process that can be easily automated). We found that the reciprocal error  $\epsilon_{N/R}$  decreased with increasing salinity of the soil water, likely due to an improved electrode contact.

**Table 3.** Mean and Standard Deviation of Residuals Between ERT- and TDR-Derived Apparent Velocity and Apparent Dispersivity at All TDR Probe Locations as a Function of the Error Level Which Constitutes Itself by the Absolute Error and the Relative Error<sup>a</sup>

$a_{app}$ ( $\Omega$ )	$b_{app}$	Error Level	$Rd_v$		$Rd_\lambda$	
			Mean (%)	SD (%)	Mean (%)	SD (%)
0.001	0.001	$\epsilon_{app} \ll \epsilon_{N/R}$	6.4	5.1	18.3	60.8
0.005	0.003	$\epsilon_{app} \approx \epsilon_{N/R}/2$	3.3	3.1	18.6	54.1
0.009	0.005	$\epsilon_{app} = \epsilon_{N/R}$	2.1	3.9	<b>17.5</b>	43.2
0.02	0.01	$\epsilon_{app} \approx 2\epsilon_{N/R}$	<b>0.2</b>	2.8	19.0	<b>26.8</b>
0.04	0.02	$\epsilon_{app} \approx 4\epsilon_{N/R}$	0.1	<b>1.6</b>	42.3	40.7
0.09	0.05	$\epsilon_{app} \gg \epsilon_{N/R}$	0	4.2	117.0	74.0

<sup>a</sup> $Rd_v$  is apparent velocity,  $Rd_\lambda$  is apparent dispersivity,  $\epsilon_{app}$  is error level,  $a_{app}$  is absolute error, and  $b_{app}$  is relative error. The best fits are shown in bold.

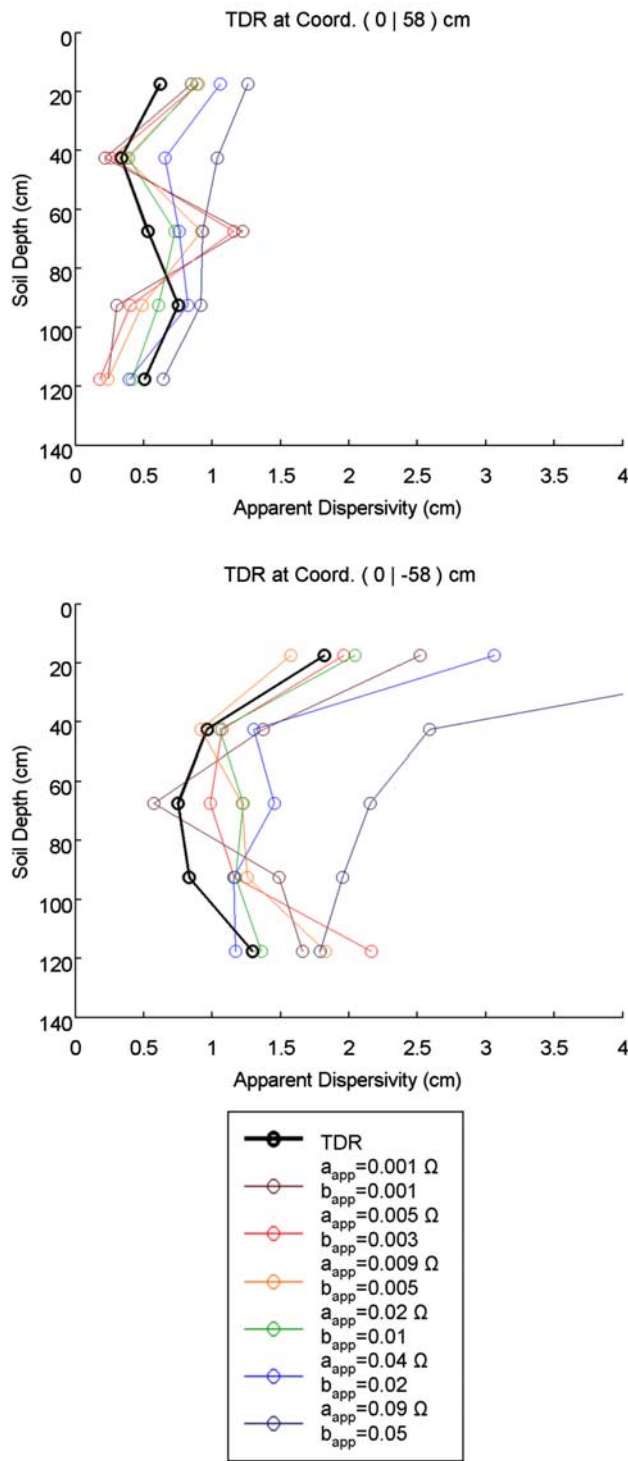


**Figure 11.** Apparent dispersivities  $\lambda_a$  (cm) from TDR and the corresponding mean of the ERT voxel BTCs as a function of  $\epsilon_{app}$ .

[80] The ERT-derived apparent transport velocities matched well with those derived from the TDR and effluent data, and the choice of the error level  $\epsilon_{app}$  was of minor importance. In contrast, the apparent dispersivities were overestimated by ERT in comparison to those determined using the TDR data. The overestimation can be explained

**Table 4.** Residuals Between ERT- and Effluent BTC-Derived Apparent Velocity and Dispersivity as a Function of the Error Level Which Constitutes Itself by the Absolute Error and the Relative Error<sup>a</sup>

$a_{app}$ ( $\Omega$ )	$b_{app}$	Error Level	$Rd_v$ (%)	$Rd_\lambda$ (%)
0.001	0.001	$\epsilon_{app} \ll \epsilon_{N/R}$	<b>0.5</b>	-22.3
0.005	0.003	$\epsilon_{app} \approx \epsilon_{N/R}/2$	1.7	-28.7
0.009	0.005	$\epsilon_{app} = \epsilon_{N/R}$	1.5	-30.3
0.02	0.01	$\epsilon_{app} \approx 2\epsilon_{N/R}$	1.3	-31.4
0.04	0.02	$\epsilon_{app} \approx 4\epsilon_{N/R}$	0.8	-27.7
0.09	0.05	$\epsilon_{app} \gg \epsilon_{N/R}$	3.9	<b>-4.3</b>

<sup>a</sup> $Rd_v$  is apparent velocity,  $Rd_\lambda$  is apparent dispersivity,  $\epsilon_{app}$  is error level,  $a_{app}$  is absolute error, and  $b_{app}$  is relative error. The best fits are shown in bold.

by the smoothness constraint used in the ERT inversion, as previously shown in synthetic studies [Kemna et al., 2002; Vanderborght et al., 2005], and temporal smearing given significant data acquisition times relative to the process dynamics. The magnitude of the overestimation was sensitive to the applied error level  $\epsilon_{app}$ . The best match was achieved for an error level  $\epsilon_{app}$  which was twice the mean reciprocal error  $\epsilon_{N/R}$ . This is in accordance with the findings of LaBrecque et al. [1996].

[81] With respect to the effluent BTC, ERT underestimated the apparent dispersivity for all applied error levels  $\epsilon_{app}$ . This is surprising as the smoothness constraint in the ERT inversion should act in the opposite direction. An explanation could be artifacts in the ERT images or effects of the water collection system at the outlet of the column. An alternative explanation is that smoothness-constrained ERT underestimated the variability of the transport velocity in the individual voxel BTCs located in regions with low sensitivity.

[82] Although we cannot verify the validity of the local-scale ERT-derived apparent transport parameters for the

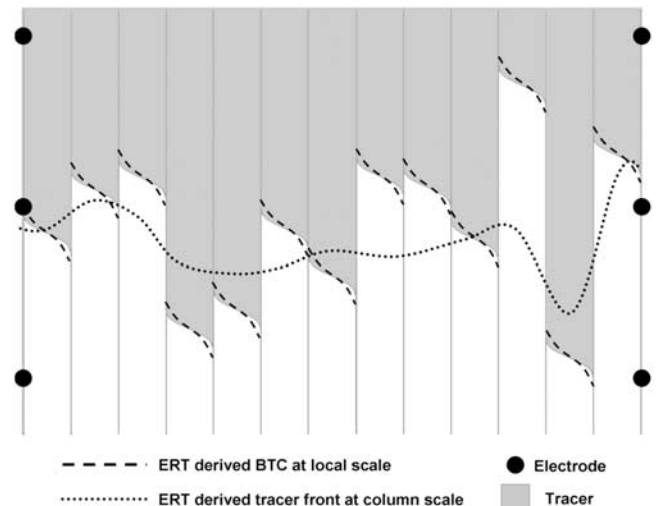


**Figure 12.** Schematic vertical cross section through the soil column illustrating how smoothness-constrained ERT is expected to image the local-scale and the column-scale BTC.

entire column, we point out that the presented approach made it possible to image a solute displacement through an undisturbed natural soil in three dimensions in a noninvasive manner with unprecedented quantitative consistency. We are positive that the experimental setup will be useful to investigate impacts of the flow rate on the 3-D solute transport characteristics.

[83] In addition, the results suggest that TDR has high potential to act as a quantitative ground truth for ERT. Furthermore, it may be possible to use TDR data to constrain the ERT inversion process. Ideally, the TDR probes should sample the entire ERT sensitivity range. Note that if ERT and TDR are applied jointly, the TDR probes should be electrically isolated from each other when ERT surveys are conducted. Otherwise, electrical short circuits, e.g., through the TDR multiplexing system, lead to severe artifacts in the ERT images.

[84] **Acknowledgments.** We thank all colleagues who helped to carry out the experiments (and carry around the considerably heavy irrigation device), especially but by no means exclusively Rainer Harms, Ansgar Weuthen, and Ferdinand Engels, as well as the staff at the ICG workshop (who built the considerably heavy but robust irrigation device). Furthermore, we would like to thank Thomas Pütz, who led the excavation survey in Kaldenkirchen and organized the transport of the monolith into the lysimeter basement. We thank Kamini Singha and two anonymous reviewers for their helpful comments and suggestions.

## References

- al Hagrey, S. A., and J. Michaelson (1999), Resistivity and percolation study of preferential flow in vadose zone at Bokhorst, Germany, *Geophysics*, *64*, 746–753, doi:10.1190/1.1444584.
- Archie, G. E. (1942), The electrical resistivity log as an aid in determining some reservoir characteristics, *Trans. Am. Inst. Min. Metall. Pet. Eng.*, *146*, 54–67.
- Biggar, J. W., and D. R. Nielsen (1976), Spatial variability of leaching characteristics of a field soil, *Water Resour. Res.*, *12*, 78–84, doi:10.1029/WR012i001p00078.
- Binley, A., and A. Kemna (2005), Electrical methods, in *Hydrogeophysics*, edited by Y. Rubin and S. S. Hubbard, pp. 129–156, Springer, New York.
- Binley, A., A. Ramirez, and W. Daily (1995), Regularised image reconstruction of noisy electrical resistance tomography data, paper presented at Workshop of the European Concerted Action on Process Tomography, Eur. Concerted Action on Process Tomogr., Bergen, Norway.
- Binley, A., S. Henry-Poulter, and B. Shaw (1996), Examination of solute transport in an undisturbed soil column using electrical resistance tomography, *Water Resour. Res.*, *32*, 763–769, doi:10.1029/95WR02995.
- Binley, A., P. Winship, L. J. West, M. Pokar, and R. Middleton (2002), Seasonal variation of moisture content in unsaturated sandstone inferred from borehole radar and resistivity profiles, *J. Hydrol.*, *267*, 160–172, doi:10.1016/S0022-1694(02)00147-6.
- Corey, J. C., D. R. Nielsen, and D. Kirkham (1967), Miscible displacement of nitrate through soil columns, *Soil Sci. Soc. Am. Proc.*, *31*, 497–501.
- Day-Lewis, F. D., K. Singha, and A. M. Binley (2005), Applying petrophysical models to radar travel time and electrical resistivity tomograms: Resolution-dependent limitations, *J. Geophys. Res.*, *110*, B08206, doi:10.1029/2004JB003569.
- De Smedt, F., F. Wauters, and J. Sevilla (1986), Study of tracer movement through unsaturated sand, *J. Hydrol.*, *85*, 169–181, doi:10.1016/0022-1694(86)90083-1.
- Deutsches Institut fuer Normung (1993), Water quality; determination of electrical conductivity, *ISO 7888:1985*, Berlin.
- Ferré, T. P. A., J. H. Knight, D. L. Rudolph, and R. G. Kachanoski (1998), The sample areas of conventional and alternative time domain reflectometry probes, *Water Resour. Res.*, *34*, 2971–2979, doi:10.1029/98WR02093.
- Franson, M. A. H. (1985), *Standard Methods for the Examination of Water and Wastewater*, 16th ed., Am. Public Health Assoc., Washington, D. C.
- French, H. K., C. Hardbattle, A. Binley, P. Winship, and L. Jakobsen (2002), Monitoring snowmelt induced unsaturated flow and transport using electrical resistivity tomography, *J. Hydrol.*, *267*, 273–284, doi:10.1016/S0022-1694(02)00156-7.
- Heimovaara, T. J. (1993), Design of triple-wire time-domain reflectometry probes in practice and theory, *Soil Sci. Soc. Am. J.*, *57*, 1410–1417.
- Heimovaara, T. J., A. G. Focke, W. Bouten, and J. M. Verstraten (1995), Assessing temporal variations in soil-water composition with time-domain reflectometry, *Soil Sci. Soc. Am. J.*, *59*, 689–698.
- Huisman, J. A., C. P. Lin, L. Weihermuller, and H. Vereecken (2008), Accuracy of bulk electrical conductivity measurements with time-domain reflectometry, *Vadose Zone J.*, *7*, 426–433, doi:10.2136/vzj2007.0139.
- Javaux, M., and M. Vanclooster (2003), Scale- and rate-dependent solute transport within an unsaturated sandy monolith, *Soil Sci. Soc. Am. J.*, *67*, 1334–1343.
- Javaux, M., J. Vanderborght, R. Kasteel, and M. Vanclooster (2006), Three-dimensional modeling of the scale- and flow rate-dependency of dispersion in a heterogeneous unsaturated sandy monolith, *Vadose Zone J.*, *5*, 515–528, doi:10.2136/vzj2005.0056.
- Jury, W. A., and K. Roth (1990), *Transfer Functions and Solute Movement Through Soil. Theory and Applications*, Birkhaeser, Basel, Switzerland.
- Kemna, A., J. Vanderborght, B. Kulesa, and H. Vereecken (2002), Imaging and characterisation of subsurface solute transport using electrical resistivity tomography (ERT) and equivalent transport models, *J. Hydrol.*, *267*, 125–146, doi:10.1016/S0022-1694(02)00145-2.
- Kemna, A., A. Binley, F. Day-Lewis, A. Englert, B. Tezkan, J. Vanderborght, H. Vereecken, and P. Winship (2006), Solute transport processes, in *Applied Hydrogeophysics*, edited by H. Vereecken et al., *NATO Sci. Ser. 4*, *71*, 117–159.
- LaBrecque, D., and S. H. Ward (1990), Two-dimensional cross-borehole resistivity model fitting, in *Geotechnical and Environmental Geophysics*, edited by S. H. Ward, pp. 51–74, Soc. of Explor. Geophys., Tulsa, Okla.
- LaBrecque, D. J., M. Mileto, W. Daily, A. Ramirez, and E. Owen (1996), The effects of noise on Occam's inversion of resistivity tomography data, *Geophysics*, *61*, 538–548, doi:10.1190/1.1443980.
- Mallants, D., M. Vanclooster, M. Meddahi, and J. Feyen (1994), Estimating solute transport in undisturbed soil columns using time-domain reflectometry, *J. Contam. Hydrol.*, *17*, 91–109, doi:10.1016/0169-7722(94)90016-7.
- Mallants, D., M. Vanclooster, N. Toride, J. Vanderborght, M. T. van Genuchten, and J. Feyen (1996), Comparison of three methods to calibrate TDR for monitoring solute movement in undisturbed soil, *Soil Sci. Soc. Am. J.*, *60*, 747–754.
- Michot, D., Y. Benderitter, A. Dorigny, B. Nicoulaud, D. King, and A. Tabbagh (2003), Spatial and temporal monitoring of soil water content with an irrigated corn crop cover using surface electrical resistivity tomography, *Water Resour. Res.*, *39*(5), 1138, doi:10.1029/2002WR001581.
- Morelli, G., and D. LaBrecque (1996), Advances in ERT modeling, *Eur. J. Environ. Eng. Geophys.*, *1*, 171–186.
- Oldenborger, G. A., P. S. Routh, and M. D. Knoll (2005), Sensitivity of electrical resistivity tomography data to electrode position errors, *Geophys. J. Int.*, *163*, 1–9, doi:10.1111/j.1365-246X.2005.02714.x.
- Olsen, P. A., A. Binley, S. Henry-Poulter, and W. Tych (1999), Characterizing solute transport in undisturbed soil cores using electrical and X-ray tomographic methods, *Hydrol. Processes*, *13*, 211–221, doi:10.1002/(SICI)1099-1085(19990215)13:2 <211::AID-HYP707 > 3.0.CO;2-P.
- Parker, J. C., and M. T. van Genuchten (1984), Flux-averaged and volume-averaged concentrations in continuum approaches to solute transport, *Water Resour. Res.*, *20*, 866–872, doi:10.1029/WR020i007p00866.
- Patterson, B. M., P. D. Franzmann, J. L. Rayner, and G. B. Davis (2000), Combining coring and suction cup data to improve the monitoring of pesticides in sandy vadose zones: A field-release experiment, *J. Contam. Hydrol.*, *46*, 187–204, doi:10.1016/S0169-7722(00)00114-5.
- Revil, A., and P. W. J. Glover (1998), Nature of surface electrical conductivity in natural sands, sandstones, and clays, *Geophys. Res. Lett.*, *25*, 691–694, doi:10.1029/98GL00296.
- Roth, K., R. Schulin, H. Flübler, and W. Attinger (1990), Calibration of time domain reflectometry for water content measurement using a composite dielectric approach, *Water Resour. Res.*, *26*, 2267–2273.
- Rothe, A., W. Weis, K. Kreutzer, D. Matthies, U. Hess, and B. Ansoerge (1997), Changes in soil structure caused by the installation of time domain reflectometry probes and their influence on the measurement of soil moisture, *Water Resour. Res.*, *33*, 1585–1593, doi:10.1029/97WR00677.
- Singha, K., and S. M. Gorelick (2005), Saline tracer visualized with three-dimensional electrical resistivity tomography: Field-scale spatial moment analysis, *Water Resour. Res.*, *41*, W05023, doi:10.1029/2004WR003460.
- Singha, K., and S. M. Gorelick (2006), Hydrogeophysical tracking of three-dimensional tracer migration: The concept and application of apparent

- petrophysical relations, *Water Resour. Res.*, *42*, W06422, doi:10.1029/2005WR004568.
- Slater, L., A. M. Binley, W. Daily, and R. Johnson (2000), Cross-hole electrical imaging of a controlled saline tracer injection, *J. Appl. Geophys.*, *44*, 85–102, doi:10.1016/S0926-9851(00)00002-1.
- Slater, L., A. Binley, R. Versteeg, G. Cassiani, R. Birken, and S. Sandberg (2002), A 3D ERT study of solute transport in a large experimental tank, *J. Appl. Geophys.*, *49*, 211–229, doi:10.1016/S0926-9851(02)00124-6.
- Topp, G. C., J. L. Davis, and A. P. Annan (1980), Electromagnetic determination of soil-water content: Measurements in coaxial transmission lines, *Water Resour. Res.*, *16*, 574–582, doi:10.1029/WR016i003p00574.
- Vanclooster, M., D. Mallants, J. Vanderborght, J. Diels, J. Vanorshoven, and J. Feyen (1995), Monitoring solute transport in a multilayered sandy lysimeter using time-domain reflectometry, *Soil Sci. Soc. Am. J.*, *59*, 337–344.
- Vanderborght, J., C. Gonzalez, M. Vanclooster, D. Mallants, and J. Feyen (1997), Effects of soil type and water flux on solute transport, *Soil Sci. Soc. Am. J.*, *61*, 372–389.
- Vanderborght, J., et al. (2001), Overview of inert tracer experiments in key Belgian soil types: Relation between transport and soil morphological and hydraulic properties, *Water Resour. Res.*, *37*, 2873–2888, doi:10.1029/2000WR000110.
- Vanderborght, J., A. Kemna, H. Hardelauf, and H. Vereecken (2005), Potential of electrical resistivity tomography to infer aquifer transport characteristics from tracer studies: A synthetic case study, *Water Resour. Res.*, *41*, W06013, doi:10.1029/2004WR003774.
- van der Pol, R. M., P. J. Wierenga, and D. R. Nielsen (1977), Solute movement in a field soil, *Soil Sci. Soc. Am. J.*, *41*, 10–13.
- Waxman, M. H., and L. J. M. Smits (1968), Electrical conductivities in oil-bearing shaly sands, *SPEJ Soc. Pet. Eng. J.*, *8*, 107–122, doi:10.2118/1863-A.
- Weihermuller, L., R. Kasteel, J. Vanderborght, T. Putz, and H. Vereecken (2005), Soil water extraction with a suction cup: Results of numerical simulations, *Vadose Zone J.*, *4*, 899–907, doi:10.2136/vzj2004.0156.
- West, L. J., K. Handley, Y. Huang, and M. Pokar (2003), Radar frequency dielectric dispersion in sandstone: Implications for determination of moisture and clay content, *Water Resour. Res.*, *39*(2), 1026, doi:10.1029/2001WR000923.
- Winship, P., A. Binley, and D. Gomez (2006), Flow and transport in the unsaturated Sherwood sandstone: Characterization using cross-borehole geophysical methods, in *Fluid Flow and Solute Movement in Sandstones: The Onshore UK Permo-Triassic Red Bed Sequence*, edited by R. D. Barker and J. H. Tellam, pp. 219–231, Geol. Soc. London, London.
- Zhou, B., and T. Dahlin (2003), Properties and effects of measurement errors on 2D resistivity imaging surveying, *Near Surf. Geophys.*, *1*, 105–117.

---

A. Binley, Lancaster Environment Centre, Lancaster University, Lancaster LA1 4YQ, UK.

M. Javaux, J. Koestel, and H. Vereecken, Agrosphere ICG-4, Forschungszentrum Jülich GmbH, D-52425 Jülich, Germany. (j.koestel@fz-juelich.de)

A. Kemna, Department of Geodynamics and Geophysics, University of Bonn, Nussalle 8, D-53115 Bonn, Germany.